JACS
JOURNAL OF THE AMERICAN CHEMICAL SOCIETY
pubs.acs.org/JACS
Article

Boosting Oxygen Electrocatalytic Activity of Fe−N−C Catalysts by Phosphorus Incorporation

Yazhou Zhou,[¶] Ruihu Lu,[¶] Xiafang Tao, Zijie Qiu, Guangbo Chen,* Juan Yang, Yan Zhao, Xinliang Feng, and Klaus Müllen*

Cite This: J. Am. Chem. Soc. 2023, 145, 3647−3655
Read Online
ACCESS | Metrics & More | Article Recommendations | Supporting Information

ABSTRACT: Nitrogen-doped graphitic carbon materials hosting single-atom iron (Fe−N−C) are major non-precious metal catalysts for the oxygen reduction reaction (ORR). The nitrogen-coordinated Fe sites are described as the first coordination sphere. As opposed to the good performance in ORR, that in the oxygen evolution reaction (OER) is extremely poor due to the sluggish O−O coupling process, thus hampering the practical applications of rechargeable zinc (Zn)−air batteries. Herein, we succeed in boosting the OER activity of Fe−N−C by additionally incorporating phosphorus atoms into the second coordination sphere, here denoted as P/Fe−N−C. The resulting material exhibits excellent OER activity in 0.1 M KOH with an overpotential as low as 304 mV at a current density of 10 mA cm^{-2}. Even more importantly, they exhibit a remarkably small ORR/OER potential gap of 0.63 V. Theoretical calculations using first-principles density functional theory suggest that the phosphorus enhances the electrocatalytic activity by balancing the *OOH/*O adsorption at the FeN_4 sites. When used as an air cathode in a rechargeable Zn−air battery, P/Fe−N−C delivers a charge−discharge performance with a high peak power density of 269 mW cm^{-2}, highlighting its role as the state-of-the-art bifunctional oxygen electrocatalyst.

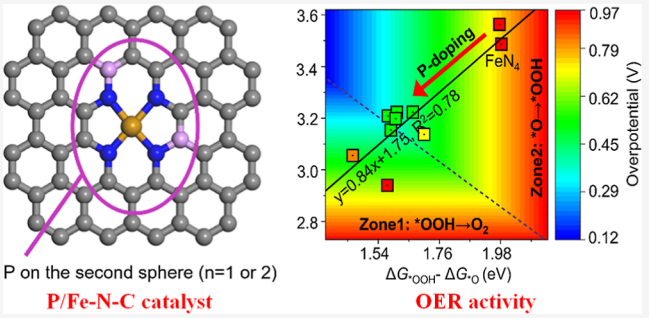

INTRODUCTION

Rechargeable zinc (Zn)−air batteries have emerged as attractive components of energy technology owing to their high energy density and environmental friendliness together with the abundance of Zn resources.[1,2] The energy efficiency of the Zn−air battery is primarily determined by the oxygen electrocatalysts of the air electrode, where the oxygen reduction reaction (ORR) and oxygen evolution reaction (OER) take place as alternating steps for discharging and charging processes, respectively.[3] However, because of their sluggish kinetics of multi-step four-electron transfer during the electrochemical process, Zn−air batteries are still hampered by very large potential gaps (>0.85 V) and low energy efficiencies.[4] To date, precious group metals (PGMs) such as platinum (Pt) and iridium (Ir) still serve as benchmark catalysts for ORR and OER,[5,6] respectively, whose high costs exclude widespread application.[7,8]

In the past decade, single-atom transition metal and nitrogen co-doped graphitic carbon (TM−N-C) materials have been developed as PGM-free catalysts with excellent ORR activity and stability in alkaline media.[9,10] The catalytically active site consists of a single transition metal center (i.e., TM) and N ligands, giving rise to TMN_xC_y units immobilized in N-doped graphitic carbon supports.[11−14] The N and C atoms are located at the first and second coordination sphere of the transition metal center, respectively[15] (Figure S1). Among PGM-free catalysts, Fe−N−C materials are the most promising catalysts for ORR.[16] FeN_4 is the most active entity whereby the Fe center adsorbs oxygen molecules and catalyzes the subsequent four-electron transfer ORR (O_2 → OOH* → O* → OH* → OH^-).[17−20] Although the newly reported Fe−N−C materials displayed a superior ORR performance than that of commercial Pt/C catalysts in alkaline solution by improving the density and accessibility of FeN_4 units and enhancing the intrinsic activity of FeN_4 for ORR by tailoring the local carbon structure (e.g., modulation by another light heteroatom),[21] their OER performance was still extremely poor.[22,23] Achieving both high ORR and OER performance on Fe−N−C is challenging but is critically important for the practical applications of these catalysts in rechargeable Zn−air batteries. The electrocatalytic activity is significantly affected by the adsorption behavior of the abovementioned oxygen-containing intermediates on the active center.[24] The reverse

Received: December 5, 2022
Published: February 6, 2023

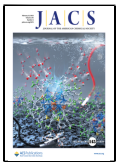

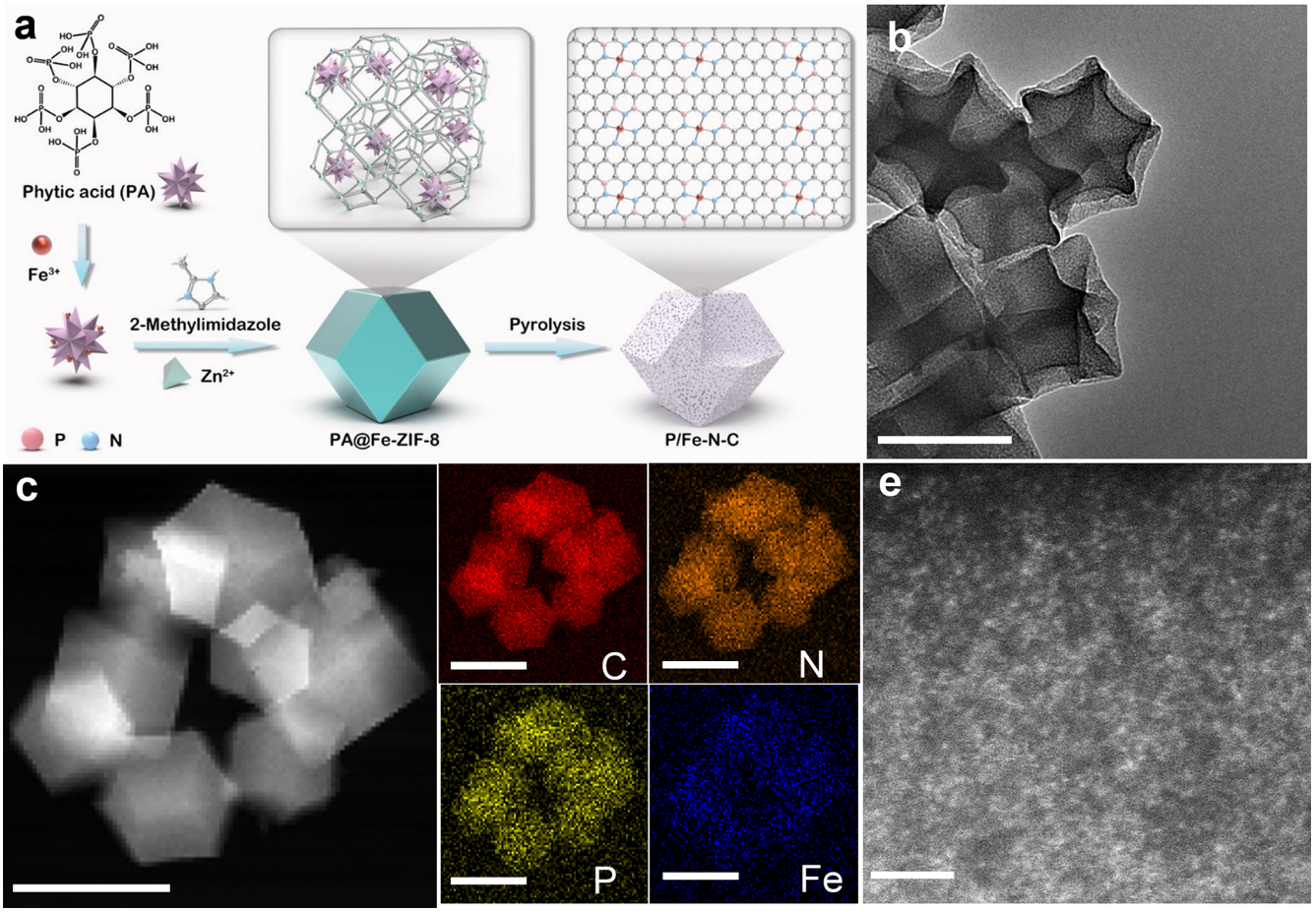

Figure 1. Synthesis and characterization of the P/Fe−N−C material. (a) Schematic illustration of the synthesis of P/Fe−N−C. (b) TEM image. (c) HAADF-STEM and (d) related elemental mapping images demonstrating the distribution of C (red), N (orange), P (yellow), and Fe (blue) elements. (e) Atomic-resolution HAADF-STEM image. Scale bar: (b−d) 150 and (e) 2 nm.

process of ORR, the OER on Fe−N−C, is kinetically sluggish mainly due to the slow O−O coupling process because of the strong O* binding strength on central Fe.[25] As a result, the catalytic conversion of *O into *OOH is the rate-determining step. Therefore, weakening the O* adsorption on the Fe center is supposed to increase the OER kinetics. Current experimental research in this direction mainly focuses on the regulation of the first or second coordination sphere, including coordination numbers, the nature of ligands,[26] and interactions between single metals.[27−29] These strategies were successfully used to promote the ORR activity.[30] Unfortunately, these strategies also weaken the OOH* adsorption, hampering the deprotonation of *OOH to release O_2 limited to the scaling relation between OH* and OOH* intermediates ($\Delta G_{OOH^*} = \Delta G_{OH^*} + 3.2 \pm 0.2$ eV), hampering the promotion of OER kinetics.[31] Therefore, balancing the *OOH/*O adsorption by weakening the O* adsorption, while at the same time enhancing the *OOH adsorption, is key for improving the OER kinetic activity on FeN_4.[32,33]

Toward that end, the Fe−N−C catalyst containing additional phosphorus incorporation was synthesized. This new material, named P/Fe−N−C, was obtained by the carbonization of the ferric phytate-modified Fe-doped zeolitic imidazolate framework (PA@Fe-ZIF-8). Spectroscopy characterization revealed that FeN_4 moieties were embedded into graphitic carbon, while phosphorus was introduced into the second coordination sphere. P/Fe−N−C delivered a significantly improved OER activity with an overpotential of only 304 mV at a current density of 10 mA cm^{-2}, as well as an excellent ORR performance in the 0.1 M KOH electrolyte. The OER activity is comparable to that of the IrO_2 benchmark (296 mV) and outperforms that of phosphorus-free Fe−N−C (450 mV). The new P/Fe−N−C catalyst, thus, qualifies as a cutting-edge bifunctional oxygen electrocatalyst. When used in an air electrode, the resulting Zn−air battery exhibited a high maximum power density of 269 mW cm^{-2} together with outstanding charge−discharge efficiency and stability. Density functional theory (DFT) calculations suggest that the presence of phosphorus results in a local distortion around Fe centers and changes the behavior of*OOH/*O adsorption. Furthermore, a new negative linear relation for *OOH/*O intermediates is found, which breaks the conventional scaling relation and balances the *OOH/*O adsorption behavior.

RESULTS AND DISCUSSION

Material Synthesis and Characterization. The synthesis of the P/Fe−N−C material is illustrated in Figure 1a. Briefly, $Fe(NO_3)_3{\cdot}6H_2O$ and phytic acid were mixed in a methanol solution to form the ferric phytates at 60 °C. Afterward, methanol solutions of $Zn(NO_3)_2{\cdot}6H_2O$ and 2-methylimidazole were added sequentially. The products, named PA@Fe-ZIF-8, were collected after reacting for 24 h. The transmission electron microscopy (TEM) image revealed dodecahedron-shaped PA@Fe-ZIF-8 nanoparticles (Figure S2). The X-ray

https://doi.org/10.1021/jacs.2c12933
J. Am. Chem. Soc. 2023, 145, 3647−3655

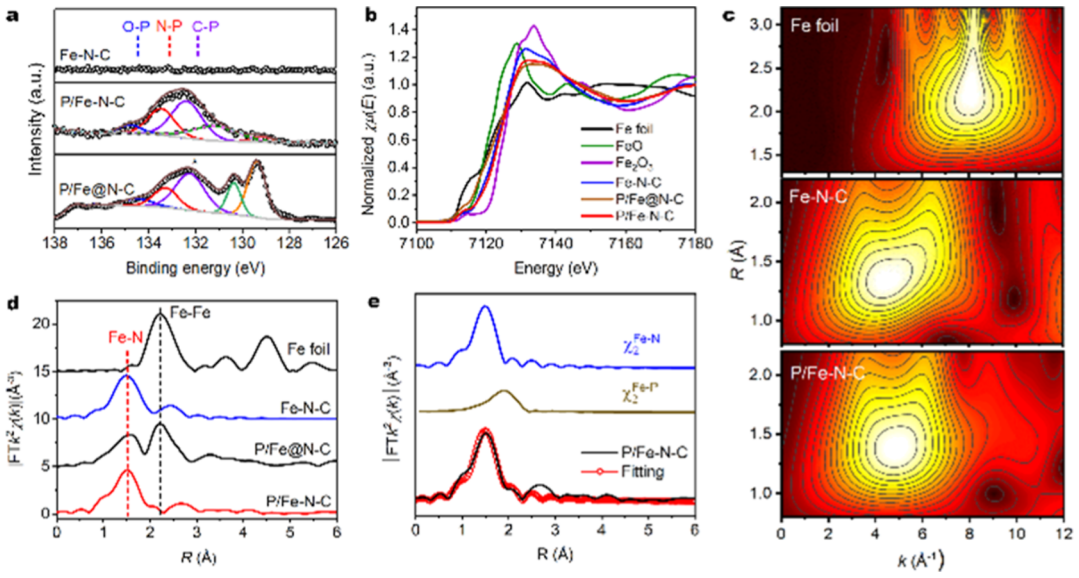

Figure 2. Structural characterization. (a) High-resolution P 2p XPS spectra of Fe−N−C, P/Fe−N−C, and P/Fe@N−C. (b) Fe K-edge XANES spectra of Fe−N−C, P/Fe−N−C, P/Fe@NC, Fe_2O_3, FeO, and Fe foil references. (c) k^3-weighted wavelet-transformed Fe K edge EXAFS spectra of Fe−N−C, P/Fe−N−C, and Fe foil. (d) k^3-weighted Fourier-transformed EXAFS spectra of Fe−N−C, P/Fe−N−C, P/Fe@NC, and Fe foil. (e) EXAFS fitting curves of P/Fe−N−C.

diffraction (XRD) analysis of PA@Fe-ZIF-8 and Fe-ZIF-8 showed identical diffraction patterns (Figure S3), indicating that the introduction of ferric phytates did not disturb the crystallization of ZIF-8. PA/Fe-ZIF-8 was then thermally treated at 1000 °C for 1 h under an Ar atmosphere. Thereby, ZIF-8 transformed into nitrogen-doped porous graphitic carbon to host single Fe atoms. Ferric phytates can not only offer a high amount of stabilized Fe atoms to form highly dispersed FeN_4 moieties but also provide phosphorus sources for the formation of the second coordination sphere around the Fe centers. The reference samples, denoted as P/Fe@N−C with Fe-based nanoparticles (Figure S4) and phosphorus-free Fe−N−C, were synthesized by identical protocols with a high loading of PA and Fe ions and without the utilization of PA, respectively (Figure S5). The detailed protocol is given in the Methods section.

The structure and morphology of the resulting Fe−N−C and P/Fe−N−C materials were first examined using scanning electron microscopy and TEM. As shown in Figures 1b and S5a, both P/Fe−N−C and Fe−N−C retained the original dodecahedron morphology of Fe-ZIF-8 particles. No Fe-containing nanoparticles (e.g., Fe and/or Fe_2P) were detected in the TEM and high-angle annular dark-field scanning TEM (HAADF-STEM) images (Figures 1c and S5b,c). Corresponding elemental mapping images revealed the homogeneous distribution of C, N, P, and Fe elements for P/Fe−N−C and the absence of P in Fe−N−C (Figures 1d and S5d,e). Furthermore, the aberration-corrected HAADF-STEM images of P/Fe−N−C and Fe−N−C indicated that Fe was atomically dispersed within the carbon support (Figures 2e and S5f). The XRD patterns of the two samples displayed two broad peaks at 24.3 and 43.7°, corresponding to the (002) and (101) planes of graphitic carbon, respectively (Figure S6). No diffraction peaks related to crystalline Fe species (e.g., Fe, Fe_3C, or Fe_3N nanoparticles) were observed. The Raman spectra of Fe−N−C and P/Fe−N−C exhibited two peaks at 1350 and 1590 cm^{-1}, corresponding to the D band (disordered sp^3 carbon) and G band (graphitic sp^2 carbon) of graphitic carbon, respectively (Figure S7). The Brunauer−Emmett−Teller surface area and the total pore volume of P/Fe−N−C were measured to be 950 $m^2\ g^{-1}$ and 1.2 $cm^3\ g^{-1}$, respectively, that is, higher than those of Fe−N−C at 684 $m^2\ g^{-1}$ and 1.0 $cm^3\ g^{-1}$, respectively (Figure S8). This could be due to gas released from the decomposition of ferric phytates, which enhanced porosity. The Fe content in P/Fe−N−C was 1.70 wt % according to inductively coupled plasma-optical emission spectroscopy and thus slightly higher than the value of 1.53 wt % for Fe−N−C.

X-ray photoelectron spectroscopy (XPS) was utilized to probe the elemental information of Fe−N−C and P/Fe−N−C (Tables S1 and S2). As depicted in Figure S9, the XPS survey spectra confirm the existence of C, N, and Fe in both materials. In contrast to Fe−N−C, a new peak located at ∼133 eV was observed, which was assigned to P 2p. The high-resolution P 2p XPS spectrum of P/Fe−N−C displays three peaks at 132.1, 133.2, and 134.3 eV (Figure 2a), which can be assigned to C−P, P−N, and P−O groups, respectively.[34] The results suggest the successful incorporation of phosphorus atoms into the graphitic carbons. The high-resolution O 1s spectrum 1s reveals the absence of the Fe−O species in the P/Fe−N−C material (Figure S10). Synchrotron-radiation-based X-ray absorption near-edge structure (XANES) and extended X-ray absorption fine structure (EXAFS) measurements were then carried out to investigate the electronic structure and coordination modes of the P/Fe−N−C, P/Fe@NC, and Fe−N−C samples. Fe K-edge XANES was first applied to analyze the oxidation state of the Fe atoms in each sample by comparing the edge position of the samples with that of standard Fe foil, FeO, and Fe_2O_3. As revealed in Figure 2b, the absorption edges of P/Fe−N−C and Fe−N−C are located in between FeO and Fe_2O_3, implying that the valence of Fe species in two samples is between 2+ and 3+.[35] Compared to Fe−N−C, P/Fe−N−C displays a positive absorption edge, suggesting a higher valence state of Fe. The presence of phosphorus atoms can thus modulate the electronic structure of the central single Fe atom of Fe−N−C materials. Fe K-edge EXAFS was applied to examine the local coordination

https://doi.org/10.1021/jacs.2c12933
J. Am. Chem. Soc. 2023, 145, 3647−3655

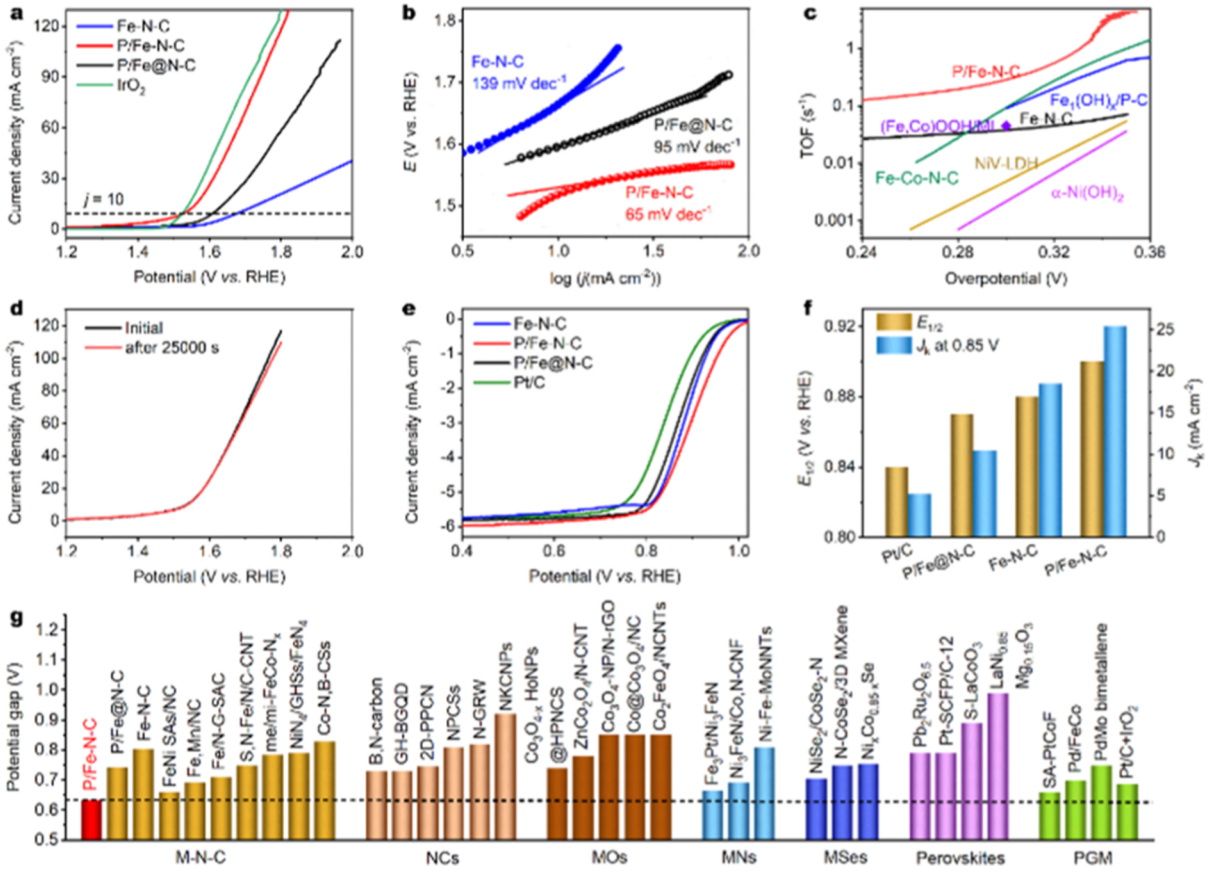

Figure 3. Electrocatalytic performance of P/Fe−N−C. (a) OER LSV curves of Fe−N−C, P/Fe−N−C, P/Fe@N−C, and IrO_2/C electrocatalysts. (b) OER Tafel plots of Fe−N−C, P/Fe−N−C, and P/Fe@N−C. (c) TOF values for OER of the P/Fe−N−C catalyst and other recently reported OER catalysts based on earth-abundant metals, including (Fe,Co)OOH/MI (ref 49), $Fe_1(OH)_x$/P−C(ref 50), NiV-LDH (ref 51), α-$Ni(OH)_2$ (ref 52), and Fe−Co−N−C (ref 53). The TOF values are based on the total amounts of metal for all catalysts. (d) LSV curves of the P/Fe−N−C electrocatalyst before and after 25,000 s stability test. (e) ORR polarization curves and (f) J_k at 0.85 V and $E_{1/2}$ for Fe−N−C, P/Fe−N−C, P/Fe@N−C, and Pt/C electrocatalysts. (g) Comparison of the potential gaps for the P/Fe−N−C and state-of-the-art bifunctional oxygen electrocatalysts. The details are shown in Table S6.

geometry of Fe sites in P/Fe−N−C and Fe−N−C. The wavelet-transformed EXAFS plots of Fe−N−C, P/Fe−N−C exhibit only one intensity maximum at ∼5.1 $Å^{-1}$ in *k* space, similar to FePc, implying an analogous Fe−N first-shell coordination (Figure 2c).[36] In the Fourier-transformed EXAFS *R*-space plot (Figure 2d), both P/Fe−N−C and Fe−N−C showed one main peak located at ∼1.52 Å, contributing to the Fe−N first coordination sphere. Compared with Fe foil and P/Fe@NC, the Fe−Fe coordination peak at ∼2.2 Å was absent in both P/Fe−N−C and Fe−N−C. This reveals the atomically dispersed nature of Fe sites.[36] EXAFS fitting analysis was adopted to determine the coordination number and interatomic bonding distance of the central Fe in P/Fe−N−C and Fe−N−C. The best-fitting result for P/Fe−N−C was obtained by using two backscattering pathways of Fe−N and Fe−P (Figure 2e), and only the Fe−N pathway can be fitted for Fe−N−C. The coordination numbers of Fe−N and Fe−P for P/Fe−N−C were calculated as 4.1 ± 0.5 and 2.2 ± 0.7 at distances of 1.97 ± 0.02 Å and 2.32 ± 0.04 Å, respectively (Table S3). Considering the coordination numbers, we proposed a configuration of FeN_4-P_n (n = 1 or 2) in which N is located in the first coordination sphere and P is located in the second coordination sphere of the Fe center. In contrast, the single-atom Fe in Fe−N−C is coordinated with four N atoms, the typical FeN_4 moiety.

OER and ORR Activities. The electrocatalytic OER performance of P−Fe−N−C was investigated by linear sweep voltammetry (LSV) using a rotating disk electrode (RDE) technique in an O_2-saturated 0.1 M KOH electrolyte solution. For comparison, a commercial IrO_2 catalyst, Fe−N−C, and P/Fe@NC were evaluated under the same conditions. All potentials were referenced to the reversible hydrogen electrode. As depicted in Figure 3a, the Fe−N−C presented a high onset OER overpotential of ∼350 mV. The result is consistent with the reported values, in which single-atom Fe−N−C materials reveal very sluggish OER kinetics.[37] In contrast, on P/Fe−N−C, oxygen generation occurred at an overpotential of only ∼130 mV, which was substantially lower than the value of ∼270 mV for the commercial IrO_2 catalyst. Outstandingly, the current density of P/Fe−N−C reached 10 mA cm^{-2} (j_{10}) at a substantially decreased overpotential of 304 mV (without *iR* compensation), which was comparable with that of IrO_2 (296 mV) and much lower than those of P/Fe@NC (384 mV) and Fe−N−C (450 mV). In addition, the Tafel slope of P/Fe−N−C was determined as ∼65 mV $decade^{-1}$, much lower than ∼88 mV $decade^{-1}$ for the IrO_2 (Figures 3b and S11). The electrochemical impedance spectroscopy of P/Fe−N−C plotted in Figure S12 further manifested a faster OER kinetic process than that of Fe−N−C. These results clearly indicate that the sluggish OER kinetics of Fe−N−C is

https://doi.org/10.1021/jacs.2c12933
J. Am. Chem. Soc. 2023, 145, 3647−3655

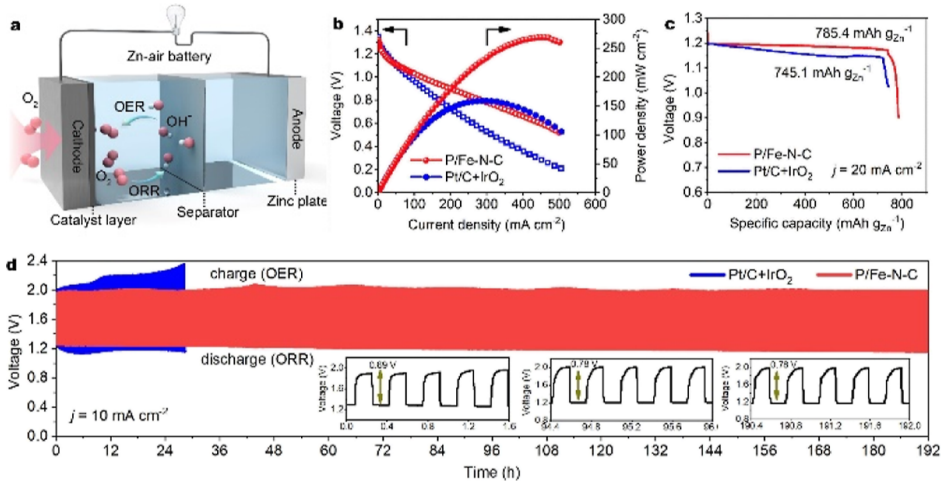

Figure 4. Rechargeable Zn−air battery performance. (a) Scheme showing the as-assembled rechargeable Zn−air battery. (b) Discharge polarization curves and corresponding power density plots of the rechargeable Zn−air batteries using the P/Fe−N−C and Pt/C−IrO_2 couple as air electrodes, respectively. (c) Zn-mass-normalized specific capacities at a current density of 20 mA cm^{-2}. (d) Discharge/charge cycling curves of Zn−air batteries using the P/Fe−N−C and Pt/C−IrO_2 couple as air electrodes at 10 mA cm^{-2}.

significantly accelerated by the incorporation of phosphorus atoms. Remarkably, the OER performance of P/Fe−N−C is superior to that of previously reported single-atom M−N-C electrocatalysts such as Fe−N_x−C (600 mV),[38] S,N−Fe/N/C-CNT (370 mV),[39] Ni-NHGF (331 mV),[40] Ni−N_4/GHSs/Fe−N_4 (390 mV),[41] Fe−Ni−N−P−C (337 mV),[42] and Fe,Mn/N−C (390 mV)[43] and even comparable or superior to those of the reported state-of-the-art metal oxides/nitrides/phosphides/selenide-based OER electrocatalysts (Table S4). Furthermore, the reaction mechanism was determined by the rotating ring-disk electrode (RRDE) technique. A very low ring current was detected, suggesting negligible hydrogen peroxide formation (Figure S13). This result means exclusive generation of O_2 during the OER process through a four-electron process, that is, $4OH^- \rightarrow O_2 + 2H_2O + 4e^-$. Moreover, the double-layer capacitance (C_{dl}) value suggests a large electrochemical active surface area of P/Fe−N−C, which would contribute to the enhanced catalytic activity (Figure S14). To evaluate the intrinsic activity of P/Fe−N−C, we estimated the turnover frequency (TOF). At an overpotential of 300 mV, the TOF of P/Fe−N−C was calculated as 0.29 s^{-1}, which is 7.6 times higher than the value for Fe−N−C (Figure 3c). Also, we compared the TOF of the P/Fe−N−C catalyst at different overpotentials with the TOF values of some recently reported non-precious-metal catalysts. Clearly, the comparison highlights P/Fe−N−C as being among the most active OER catalysts with the highest atom utilization efficiency. Catalytic durability is another vital criterion for evaluating the OER performance of an electrocatalyst which was determined by holding a constant current density (i.e., j_{10}) for 25,000 s (Figure S15). As revealed in Figure 3d, the OER overpotential of the P/Fe−N−C at j_{10} increased by only 2 mV. Some loss of activity was observed after holding at a constant voltage of 1.53 V for 10 h. The structural and chemical compositional changes in the P/Fe−N−C after the durability tests were examined using Raman spectroscopy, XPS (Figure S16), and HRTEM analyses (Figure S17).

The electrocatalytic ORR tests of P/Fe−N−C were also conducted by the RDE technique in a 0.1 M KOH employing a commercial Pt/C catalyst (20% Pt, Fuelcellstore), Fe−N−C, and P/Fe@N−C as references. As shown in Figure 3e, Fe−N−C displayed excellent ORR performance with an onset potential of 0.99 V. The ORR activity of P/Fe−N−C was slightly improved with an onset potential of 1.01 V. Noticeably, a half-wave potential ($E_{1/2}$) of 0.90 V was higher than those of 0.88 V for Fe−N−C, 0.87 V for P/Fe@N−C, and 0.84 V for Pt/C benchmark. In addition, the kinetic current density (J_k) of the P/Fe−N−C reached 25.4 mA cm^{-2} at 0.85 V, which was 4.9 times higher than the value for Pt/C (Figure 3f). Using the RRDE method, the H_2O_2 yield of the P/Fe−N−C sample was determined as <1.5% in a potential range from 0.4 to 0.9 V. The corresponding electron-transfer number was larger than 3.9 (Figure S18), suggesting the desired four-electron ORR process. In addition, the P/Fe−N−C material presented good ORR stability (Figure S19). The site density for ORR was quantified by the in situ electrochemical method by means of nitrite absorption followed by reductive stripping. The corresponding TOF was then evaluated based on the stripping charge. The P/Fe−N−C displayed a higher site density of 21.8 μmol g^{-1} and a lower TOF of 2.0 s^{-1} at 0.85 V compared to those of Fe−N−C (13.9 μmol g^{-1} and 2.5 s^{-1}) (Figure S20 and Table S5). These results indicate that the slightly enhanced ORR activity of P/Fe−N−C can mainly be attributed to the high intrinsic activity and increased density of active sites as a result of high Fe loading and surface area.

The bifunctional oxygen electrocatalytic performance of P/Fe−N−C was estimated by calculating the potential gap (ΔE) between the OER potential at 10 mA cm^{-2} ($E_{j=10}$) and ORR $E_{1/2}$. Remarkably, the P/Fe−N−C demonstrated a small ΔE of 0.63 V, and thus, it was substantially lower than the value of 0.69 V for the Pt/C−IrO_2 couple and those for state-of-the-art bifunctional oxygen electrocatalysts including single-atom M-N-C, metal-free materials, metal oxides/nitrides/phosphides/selenides, perovskites, and PGM-based electrodes (Figure 3g and Table S6). Representative examples are 0.69 V for Fe,Mn/NC,[43] 0.73 V for B-doped graphene quantum dots anchored on a graphene hydrogel (GH-BGQD),[44] 0.74 V for Co_3O_{4-x} HoNPs@HPNCS,[45] 0.69 V for Ni_3FeN/Co,N−CNF,[46] 0.79 V for $Pb_2Ru_2O_{6.5}$,[47] and 0.75 V for PdMo bimetallene.[48] These results implied that the P/Fe−N−C is one of the best candidates for bifunctional oxygen electrocatalysis.

https://doi.org/10.1021/jacs.2c12933
J. Am. Chem. Soc. 2023, 145, 3647−3655

Rechargeable Zn−Air Battery Performance. To evaluate its practical application in energy devices, a rechargeable Zn−air battery was assembled utilizing P/Fe−N−C as the oxygen catalyst of the air electrode in a 6.0 M KOH electrolyte containing 0.2 M $Zn(OAc)_2$ (Figure 4a). A reference Zn−air battery was also constructed and tested by using a Pt/C + IrO_2 coupled catalyst (with the same mass ratio) as the air electrode. As shown in Figure S17, the open-circuit voltage of the P/Fe−N−C reached 1.48 V. The corresponding maximum power density of the P/Fe−N−C-based battery was 269 mW cm^{-2} and higher than that of Pt/C + IrO_2 (159 mW cm^{-2}) (Figure 4b). It delivered a specific capacity of 785 mA h g_{Zn}^{-1} at a discharge current density of 20 mA cm^{-2}, corresponding to ∼96% utilization of the theoretical capacity (∼820 mA h g_{Zn}^{-1})[39] (Figure 4c). To investigate the cycling performance of the Zn−air batteries, the galvanostatic charge and discharge test was performed at 10 mA cm^{-2} with 20 min per cycle (10 min for discharge, 10 min for charge). After 96 h, the potential gap for charge and discharge only increased by 0.09 V. Then there was no noticeable degradation over 192 h, suggesting good electrocatalytic durability in the alternative OER and ORR processes (Figure 4d). In sharp contrast, the battery with the Pt/C + IrO_2 catalyst lost its activity after 500 cycles.

Theoretical Investigation of the Role of Phosphorus. First-principles DFT calculations were conducted to shed light on the influence of phosphorus on the OER activity of P/Fe−N−C. We constructed 23 possible structures. Two kinds of models were considered, comprising one or two phosphorus atoms within the second coordination sphere of the Fe center (i.e., FeN_4−P_1 and FeN_4−P_2) (Figure S21). By screening the bond length and energy of formation for the Fe−P bond, nine models (Table S7) were fitted for our experimental analysis. A local distortion was found due to the larger atomic radius of the phosphorus atom with respect to carbon. This induces structural distortions depending upon the number and position of P-dopants together with lengthening the Fe−N bonds (Table S8) and generates tensile strain. Strain effects represent an efficient strategy to tune the local environment of active sites and thus the oxygen binding ability.[31,33] The adsorption behavior of the OER intermediates (i.e., OH*, O*, and OOH*) on the catalyst models was examined (Table S9), and the corresponding Gibbs free energy profiles for the OER are displayed in Figure S22. It can be concluded from Figure 5a that the OER activity on all the catalyst models can be described as a function of the Gibbs adsorption energies ($\Delta G_{*OOH} - \Delta G_{*O}$) and ΔG_{*OOH}. The former corresponds to the steps of O−O coupling (*O → *OOH), and latter corresponds to O_2 release (*OOH → O_2). On pristine Fe−N−C, the OER overpotential is as large as 0.92 eV for O−O coupling. This explains the poor OER activity of the reported Fe−N−C materials.[40] In contrast, in all P/Fe−N−C models, the OER activities are improved, benefitting from the increased ΔG_{*OOH} and decreased ($\Delta G_{*OOH} - \Delta G_{*O}$) values. The effect of alternative structures in the P/Fe−N−C catalyst on OER activity was also investigated, including vacancy defects, N doping, P doping, N, P co-doping, dual-atom Fe, and P-doped Fe−N−C, which contain different distances between Fe and P atoms (Figures S23−S27 and Tables S10 and S11). One can conclude that the introduction of phosphorus into the second coordination sphere of the Fe center leads to an optimal OER performance by tuning the *OOH/*O adsorption. One can conclude that the introduction of phosphorus into the second coordination sphere of the Fe center leads to an optimal OER performance by tuning the *OOH/*O adsorption.

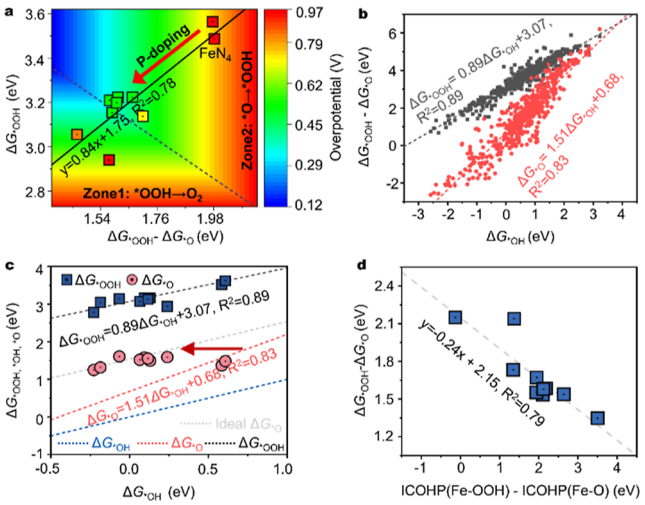

Figure 5. Fundamental understanding of the P effect on Fe active sites by using DFT calculations. (a) Contour plot of OER overpotential as a function of Gibbs adsorption energies [($\Delta G_{*OOH} - \Delta G_{*O}$) along the *x*-axis and ΔG_{*OOH} along the *y*-axis]. The inset is the scaling relation $\Delta G_{*OOH} = 0.84\ (\Delta G_{*OOH} - \Delta G_{*O}) + 1.75$. (b) Scaling relations of adsorption energies among OER intermediates. The blue, red, and black dashed lines are obtained by fitting data from previous studies, and the gray dashed line is the middle line between ΔG_{*OOH} and ΔG_{*OH}, indicating the ideal line of ΔG_{*O}. (c) Scaling relation of adsorption energies for different OER intermediates on the P/Fe−N−C. The dotted line denotes the statistics scaling relation on TM-N_4C_{12} originated in figure b. (d) Linear relation between ICOHP(Fe−OOH) − ICOHP(Fe−O) and $\Delta G_{*OOH} - \Delta G_{*O}$.

To further understand the mechanism of augmented OER activity, the change in *OOH/*O adsorption behavior was investigated. We collected approximately 500 pieces of data from reference papers to plot relatively precise scaling relations of TMN_4-C_{12} configuration in Figure 5b and the dashed line in Figure 5c. They are $\Delta G_{*OOH} = 0.89\Delta G_{*OH} + 3.07$, $R^2 = 0.89$ and $\Delta G_{*O} = 1.51\Delta G_{*OH} + 0.68$, $R^2 = 0.83$, respectively. These scaling relations slightly differ from the reported one, that is, $\Delta G_{OOH*} = \Delta G_{OH*} + 3.2$ on metal oxide.[54] Generally, an ideal OER catalyst should have an optimal ΔG_{*O} value between ΔG_{*OH} and ΔG_{*OOH}. When plotting ΔG_{*O} versus ΔG_{*OH} (1.51) for the single-atom catalysts, ΔG_{*O} deviates more from the value between ΔG_{*OH} and ΔG_{*OOH}. Therefore, these catalysts exhibit a large difference of ($\Delta G_{*O} - \Delta G_{*OOH}$) and a high OER overpotential. This is in good agreement with the big change in free energy by converting *O into *OOH (Figure S22), indicating a sluggish O−O coupling process on Fe−N−C. The newly linear correlation between $\Delta G_{*OOH} - \Delta G_{*O}$ and ΔG_{*OOH}: $\Delta G_{*OOH} = 0.84\ (\Delta G_{*OOH} - \Delta G_{*O}) + 1.75$, $R^2 = 0.78$ on P/Fe−N−C systems (Figure 5a) implies that the ΔG_{*OOH} is negatively correlated with ΔG_{*O}. This differs from predictions of earlier scaling relations.[33] It can be seen from Figure 5c that the *OOH adsorption energies on P/Fe−N−C still fulfill the scaling relations of TMN_4-C_{12}, whereas most *O adsorption energies approach the mean value of ΔG_{*OOH} and ΔG_{*OH}. We further calculated the *OOH, *OH, and *O free energies of adsorption in the theoretical framework of DFT + U. The results were consistent with the DFT calculation (Figure S28 and Table S12). Thus, the different response of *OOH/*O adsorption to the local

https://doi.org/10.1021/jacs.2c12933
J. Am. Chem. Soc. 2023, 145, 3647−3655

distortion around the Fe center is caused by phosphorus, which then prompts a higher OER activity of FeN_4. We further calculated the integrated crystal orbital Hamilton population (ICOHP), which is an effective measure of the bonding strength.[55] The difference $\Delta G_{*OOH} - \Delta G_{*O}$ varies linearly with the difference between ICOHP(Fe−OOH) and ICOHP(Fe−O) (Figure 5d). This implies that different responses of OOH/*O adsorption are due to the different binding abilities of *OOH/*O on Fe sites.[23] In brief, the presence of the phosphorus atom in the second coordination sphere causes a local distortion on the central Fe and tensile strain, which balances the *OOH/*O adsorption characteristics and accordingly facilitates the OER process.

CONCLUSIONS

In summary, we introduce a new single-atom P/Fe−N−C material for rechargeable Zn−air batteries by a phosphorus incorporation protocol. Comprehensive spectroscopic characterization suggests that the phosphorus atom is located in the second coordination sphere of the Fe center. The achieved P/Fe−N−C exhibits excellent OER activity in alkaline media, approaching benchmark IrO_2, as well as high ORR activity. As a result, the P/Fe−N−C provides state-of-the-art performance as a bifunctional oxygen electrocatalyst for a rechargeable Zn−air battery. According to DFT calculations, the presence of phosphorus efficiently improves the kinetics of O−O formation and breaks the traditional scaling relationship. These results (i) provide a deeper mechanistic understanding of Fe−N−C materials in electrocatalytic oxygen reactions, (ii) are prone to improving the performance in acidic solution by incorporation of heteroatoms, and (iii) will stimulate the search for single-atom catalysts of other electrochemical reactions such as water splitting, CO_2 reduction, and nitrogen fixation.

ASSOCIATED CONTENT

Supporting Information

The Supporting Information is available free of charge at https://pubs.acs.org/doi/10.1021/jacs.2c12933.

Detailed experimental and characterization methods; schematic of the SAC with first and second coordination spheres; morphologies and crystalline structures of Fe−N−C, P/Fe@N−C, and P/Fe−N−C before and after pyrolysis; Raman spectra; N_2 adsorption/desorption isotherms; XPS analysis; EXAFS fitting results; OER Tafel plot; EIS analysis; OER performance comparison; CV curves; i−t curve; structural changes after catalytic performance; ORR selectivity analysis and ORR stability; determination of the Fe site density; potential gaps between OER and ORR; possible P-doping Fe−N−C (1-23) and pure Fe−N−C catalysts; Fe-P bonds and formation energy; Fe−N bond lengths and corresponding strain in the P/Fe−N−C material; adsorption energies, free energy changes, overpotential, and the difference of ICOHP; free-energy diagrams; optimal models of possible active sites; correlation between the OER activity and ORR activity; and scaling relation of adsorption energies (PDF)

AUTHOR INFORMATION

Corresponding Authors

Guangbo Chen − *Center for Advancing Electronics Dresden (Cfaed) and Faculty of Chemistry and Food Chemistry, Technische Universität Dresden, Dresden 01062, Germany*; Email: guangbo.chen@tu-dresden.de

Klaus Müllen − *Max Planck Institute for Polymer Research, Mainz 55128, Germany*; orcid.org/0000-0001-6630-8786; Email: muellen@mpip-mainz.mpg.de

Authors

Yazhou Zhou − *Max Planck Institute for Polymer Research, Mainz 55128, Germany; School of Materials Science and Engineering, Jiangsu University, Zhenjiang 212013 Jiangsu, China*; orcid.org/0000-0002-0446-2291

Ruihu Lu − *State Key Laboratory of Silicate Materials for Architectures, International School of Materials Science and Engineering, Wuhan University of Technology, Wuhan 430070 Hubei, China*; orcid.org/0000-0001-8405-5962

Xiafang Tao − *Max Planck Institute for Polymer Research, Mainz 55128, Germany; School of Materials Science and Engineering, Jiangsu University, Zhenjiang 212013 Jiangsu, China*

Zijie Qiu − *Max Planck Institute for Polymer Research, Mainz 55128, Germany; School of Science and Engineering, Shenzhen Institute of Aggregate Science and Technology, The Chinese University of Hong Kong, Shenzhen 518172 Guangdong, China*; orcid.org/0000-0003-0728-1178

Juan Yang − *School of Materials Science and Engineering, Jiangsu University, Zhenjiang 212013 Jiangsu, China*; orcid.org/0000-0003-0118-7084

Yan Zhao − *State Key Laboratory of Silicate Materials for Architectures, International School of Materials Science and Engineering, Wuhan University of Technology, Wuhan 430070 Hubei, China*; orcid.org/0000-0002-1234-4455

Xinliang Feng − *Center for Advancing Electronics Dresden (Cfaed) and Faculty of Chemistry and Food Chemistry, Technische Universität Dresden, Dresden 01062, Germany; Max Planck Institute of Microstructure Physics, Halle (Saale) D-06120, Germany*; orcid.org/0000-0003-3885-2703

Complete contact information is available at: https://pubs.acs.org/10.1021/jacs.2c12933

Author Contributions

[¶]Y.Z. and R.L. contributed equally.

Funding

Open access funded by Max Planck Society.

Notes

The authors declare no competing financial interest.

ACKNOWLEDGMENTS

We thank the financial support from the Max Planck Society, European Research Council (ERC) under the European Union's Horizon 2020 research and innovation program (no 819698 and GrapheneCore3: 881603), Deutsche Forschungsgemeinschaft (CRC 1415: 417590517). Y.Z. and J.Y. thank the Natural Science Foundation of China (5170212 and 51972150). Y.Z. acknowledges the China Postdoctoral Science Foundation (2018M630527 and 2019T120459) and the China Scholarship Council for financial support (201708320150).

REFERENCES

(1) Fu, J.; Cano, Z. P.; Park, M. G.; Yu, A.; Fowler, M.; Chen, Z. Electrically rechargeable zinc-air batteries: progress, challenges, and perspectives. *Adv. Mater.* **2017**, *29*, 1604685.

(2) Lee, J.-S.; Tai Kim, S.; Cao, R.; Choi, N.-S.; Liu, M.; Lee, K. T.; Cho, J. Metal-air batteries with high energy density: Li-air versus Zn-air. *Adv. Energy Mater.* **2011**, *1*, 34−50.

(3) Li, Y.; Dai, H. Recent advances in zinc-air batteries. *Chem. Soc. Rev.* **2014**, *43*, 5257−5275.

(4) Leong, K. W.; Wang, Y.; Ni, M.; Pan, W.; Luo, S.; Leung, D. Y. C. Rechargeable Zn-air batteries: recent trends and future perspectives. *Renewable Sustainable Energy Rev.* **2022**, *154*, 111771.

(5) Seh, Z. W.; Kibsgaard, J.; Dickens, C. F.; Chorkendorff, I.; Nørskov, J. K.; Jaramillo, T. F. Combining theory and experiment in electrocatalysis: Insights into materials design. *Science* **2017**, *355*, No. eaad4998.

(6) Zhu, Z.; Jiang, T.; Ali, M.; Meng, Y.; Jin, Y.; Cui, Y.; Chen, W. Rechargeable Batteries for Grid Scale Energy Storage. *Chem. Rev.* **2022**, *122*, 16610−16751.

(7) Dai, L.; Xue, Y.; Qu, L.; Choi, H.-J.; Baek, J.-B. Metal-free catalysts for oxygen reduction reaction. *Chem. Rev.* **2015**, *115*, 4823−4892.

(8) Jiao, Y.; Zheng, Y.; Jaroniec, M.; Qiao, S. Z. Design of electrocatalysts for oxygen- and hydrogen-involving energy conversion reactions. *Chem. Soc. Rev.* **2015**, *44*, 2060−2086.

(9) Wan, C.; Duan, X.; Huang, Y. Molecular design of single-atom catalysts for oxygen reduction reaction. *Adv. Energy Mater.* **2020**, *10*, 1903815.

(10) Adabi, H.; Shakouri, A.; Ul Hassan, N.; Varcoe, J. R.; Zulevi, B.; Serov, A.; Regalbuto, J. R.; Mustain, W. E. High-performing commercial Fe-N-C cathode electrocatalyst for anion-exchange membrane fuel cells. *Nat. Energy* **2021**, *6*, 834−843.

(11) Chen, G.; Zhong, H.; Feng, X. Active site engineering of single-atom carbonaceous electrocatalysts for the oxygen reduction reaction. *Chem. Sci.* **2021**, *12*, 15802−15820.

(12) Ji, S.; Jiang, B.; Hao, H.; Chen, Y.; Dong, J.; Mao, Y.; Zhang, Z.; Gao, R.; Chen, W.; Zhang, R.; Liang, Q.; Li, H.; Liu, S.; Wang, Y.; Zhang, Q.; Gu, L.; Duan, D.; Liang, M.; Wang, D.; Yan, X.; Li, Y. Matching the kinetics of natural enzymes with a single-atom iron nanozyme. *Nat. Catal.* **2021**, *4*, 407−417.

(13) Wan, J.; Zhao, Z.; Shang, H.; Peng, B.; Chen, W.; Pei, J.; Zheng, L.; Dong, J.; Cao, R.; Sarangi, R.; Jiang, Z.; Zhou, D.; Zhuang, Z.; Zhang, J.; Wang, D.; Li, Y. In Situ Phosphatizing of Triphenylphosphine Encapsulated within Metal−Organic Frameworks to Design Atomic Co1−P1N3 Interfacial Structure for Promoting Catalytic Performance. *J. Am. Chem. Soc.* **2020**, *142*, 8431−8439.

(14) Hu, B.; Huang, A.; Zhang, X.; Chen, Z.; Tu, R.; Zhu, W.; Zhuang, Z.; Chen, C.; Peng, Q.; Li, Y. Atomic Co/Ni dual sites with N/P-coordination as bifunctional oxygen electrocatalyst for rechargeable zinc-air batteries. *Nano Res.* **2021**, *14*, 3482−3488.

(15) Kim, J.; Yoo, J. M.; Lee, H. S.; Sung, Y.-E.; Hyeon, T. Single-atom M−N−C catalysts for oxygen reduction electrocatalysis. *Trends Chem.* **2021**, *3*, 779−794.

(16) Wang, Y.; Su, H.; He, Y.; Li, L.; Zhu, S.; Shen, H.; Xie, P.; Fu, X.; Zhou, G.; Feng, C.; Zhao, D.; Xiao, F.; Zhu, X.; Zeng, Y.; Shao, M.; Chen, S.; Wu, G.; Zeng, J.; Wang, C. Advanced Electrocatalysts with Single-Metal-Atom Active Sites. *Chem. Rev.* **2020**, *120*, 12217−12314.

(17) Chung, H. T.; Cullen, D. A.; Higgins, D.; Sneed, B. T.; Holby, E. F.; More, K. L.; Zelenay, P. Direct atomic-level insight into the active sites of a high-performance PGM-free ORR catalyst. *Science* **2017**, *357*, 479−484.

(18) Zitolo, A.; Goellner, V.; Armel, V.; Sougrati, M.-T.; Mineva, T.; Stievano, L.; Fonda, E.; Jaouen, F. Identification of catalytic sites for oxygen reduction in iron- and nitrogen-doped graphene materials. *Nat. Mater.* **2015**, *14*, 937−942.

(19) He, Y.; Liu, S.; Priest, C.; Shi, Q.; Wu, G. Atomically dispersed metal−nitrogen−carbon catalysts for fuel cells: advances in catalyst design, electrode performance, and durability improvement. *Chem. Soc. Rev.* **2020**, *49*, 3484−3524.

(20) Zhou, Y.; Chen, G.; Wang, Q.; Wang, D.; Tao, X.; Zhang, T.; Feng, X.; Müllen, K. Fe-N-C Electrocatalysts with Densely Accessible Fe-N_4 Sites for Efficient Oxygen Reduction Reaction. *Adv. Funct. Mater.* **2021**, *31*, 2102420.

(21) Li, K.; Zhang, S.; Zhang, X.; Liu, S.; Jiang, H.; Jiang, T.; Shen, C.; Yu, Y.; Chen, W. Atomic Tuning of Single-Atom Fe−N−C Catalysts with Phosphorus for Robust Electrochemical CO2 Reduction. *Nano Lett.* **2022**, *22*, 1557−1565.

(22) Ji, S.; Chen, Y.; Wang, X.; Zhang, Z.; Wang, D.; Li, Y. Chemical synthesis of single atomic site catalysts. *Chem. Rev.* **2020**, *120*, 11900−11955.

(23) Lee, W. H.; Ko, Y.-J.; Kim, J.-Y.; Min, B. K.; Hwang, Y. J.; Oh, H.-S. Single-atom catalysts for the oxygen evolution reaction: recent developments and future perspectives. *Chem. Commun.* **2020**, *56*, 12687−12697.

(24) Wang, Q.; Shang, L.; Sun-Waterhouse, D.; Zhang, T.; Waterhouse, G. Engineering local coordination environments and site densities for high-performance Fe-N-C oxygen reduction reaction electrocatalysis. *SmartMat* **2021**, *2*, 154−175.

(25) Ou, H.; Wang, D.; Li, Y. How to select effective electrocatalysts: Nano or single atom? *Nano Sel.* **2021**, *2*, 492−511.

(26) Chen, Y.; Ji, S.; Chen, C.; Peng, Q.; Wang, D.; Li, Y. Single-Atom Catalysts: Synthetic Strategies and Electrochemical Applications. *Joule* **2018**, *2*, 1242−1264.

(27) Shan, J.; Ye, C.; Jiang, Y.; Jaroniec, M.; Zheng, Y.; Qiao, S.-Z. Metal-metal interactions in correlated single-atom catalysts. *Sci. Adv.* **2022**, *8*, No. eabo0762.

(28) Tang, C.; Chen, L.; Li, H.; Li, L.; Jiao, Y.; Zheng, Y.; Xu, H.; Davey, K.; Qiao, S.-Z. Tailoring Acidic Oxygen Reduction Selectivity on Single-Atom Catalysts via Modification of First and Second Coordination Spheres. *J. Am. Chem. Soc.* **2021**, *143*, 7819−7827.

(29) Zhang, W.; Fu, Q.; Luo, Q.; Sheng, L.; Yang, J. Understanding Single-Atom Catalysis in View of Theory. *JACS Au* **2021**, *1*, 2130−2145.

(30) Qin, J.; Liu, H.; Zou, P.; Zhang, R.; Wang, C.; Xin, H. L. Altering Ligand Fields in Single-Atom Sites through Second-Shell Anion Modulation Boosts the Oxygen Reduction Reaction. *J. Am. Chem. Soc.* **2022**, *144*, 2197−2207.

(31) Huang, Z.-F.; Song, J.; Dou, S.; Li, X.; Wang, J.; Wang, X. Strategies to break the scaling relation toward enhanced oxygen electrocatalysis. *Matter* **2019**, *1*, 1494−1518.

(32) Cheng, M.-J.; Head-Gordon, M.; Bell, A. T. How to chemically tailor metal-porphyrin-like active sites on carbon nanotubes and graphene for minimal overpotential in the electrochemical oxygen evolution and oxygen reduction reactions. *J. Phys. Chem. C* **2014**, *118*, 29482−29491.

(33) Khorshidi, A.; Violet, J.; Hashemi, J.; Peterson, A. A. How strain can break the scaling relations of catalysis. *Nat. Catal.* **2018**, *1*, 263−268.

(34) Yuan, K.; Lützenkirchen-Hecht, D.; Li, L.; Shuai, L.; Li, Y.; Cao, R.; Qiu, M.; Zhuang, X.; Leung, M. K. H.; Chen, Y.; Scherf, U. Boosting Oxygen Reduction of Single Iron Active Sites via Geometric and Electronic Engineering: Nitrogen and Phosphorus Dual Coordination. *J. Am. Chem. Soc.* **2020**, *142*, 2404−2412.

(35) Gu, J.; Hsu, C.-S.; Bai, L.; Chen, H. M.; Hu, X. Atomically dispersed Fe^{3+} sites catalyze efficient CO_2 electroreduction to CO. *Science* **2019**, *364*, 1091−1094.

(36) Wang, Q.; Yang, Y.; Sun, F.; Chen, G.; Wang, J.; Peng, L.; Chen, W.-T.; Shang, L.; Zhao, J.; Sun-Waterhouse, D.; Zhang, T.; Waterhouse, G. I. N. Molten NaCl-Assisted Synthesis of Porous Fe-N-C Electrocatalysts with a High Density of Catalytically Accessible FeN4 Active Sites and Outstanding Oxygen Reduction Reaction Performance. *Adv. Energy Mater.* **2021**, *11*, 2100219.

(37) Peng, L.; Shang, L.; Zhang, T.; Waterhouse, G. I. N. Recent advances in the development of single-atom catalysts for oxygen electrocatalysis and zinc-air batteries. *Adv. Energy Mater.* **2020**, *10*, 2003018.

https://doi.org/10.1021/jacs.2c12933
J. Am. Chem. Soc. 2023, 145, 3647−3655

(38) Han, J.; Meng, X.; Lu, L.; Bian, J.; Li, Z.; Sun, C. Single-atom Fe-N_x-C as an efficient electrocatalyst for Zinc-air batteries. *Adv. Funct. Mater.* **2019**, *29*, 1808872.
(39) Chen, P.; Zhou, T.; Xing, L.; Xu, K.; Tong, Y.; Xie, H.; Zhang, L.; Yan, W.; Chu, W.; Wu, C.; Xie, Y. Atomically dispersed iron-nitrogen species as electrocatalysts for bifunctional oxygen evolution and reduction reactions. *Angew. Chem., Int. Ed.* **2017**, *56*, 610−614.
(40) Fei, H.; Dong, J.; Feng, Y.; Allen, C. S.; Wan, C.; Volosskiy, B.; Li, M.; Zhao, Z.; Wang, Y.; Sun, H.; An, P.; Chen, W.; Guo, Z.; Lee, C.; Chen, D.; Shakir, I.; Liu, M.; Hu, T.; Li, Y.; Kirkland, A. I.; Duan, X.; Huang, Y. General synthesis and definitive structural identification of MN_4C_4 single-atom catalysts with tunable electrocatalytic activities. *Nat. Catal.* **2018**, *1*, 63−72.
(41) Chen, J.; Li, H.; Fan, C.; Meng, Q.; Tang, Y.; Qiu, X.; Fu, G.; Ma, T. Dual single-atomic Ni-N_4 and Fe-N_4 sites constructing janus hollow graphene for selective oxygen electrocatalysis. *Adv. Mater.* **2020**, *32*, 2003134.
(42) Pan, F.; Jin, T.; Yang, W.; Li, H.; Cao, Y.; Hu, J.; Zhou, X.; Liu, H.; Duan, X. Theory-guided design of atomic Fe-Ni dual sites in N,P-co-doped C for boosting oxygen evolution reaction. *Chem. Catal.* **2021**, *1*, 734−745.
(43) Yang, G.; Zhu, J.; Yuan, P.; Hu, Y.; Qu, G.; Lu, B.-A.; Xue, X.; Yin, H.; Cheng, W.; Cheng, J.; Xu, W.; Li, J.; Hu, J.; Mu, S.; Zhang, J.-N. Regulating Fe-spin state by atomically dispersed Mn-N in Fe-N-C catalysts with high oxygen reduction activity. *Nat. Commun.* **2021**, *12*, 1734.
(44) Tam, T. V.; Kang, S. G.; Kim, M. H.; Lee, S. G.; Hur, S. H.; Chung, J. S.; Choi, W. M. Novel graphene hydrogel/B-doped graphene quantum dots composites as trifunctional electrocatalysts for Zn-air batteries and overall water splitting. *Adv. Energy Mater.* **2019**, *9*, 1900945.
(45) Ji, D.; Fan, L.; Tao, L.; Sun, Y.; Li, M.; Yang, G.; Tran, T. Q.; Ramakrishna, S.; Guo, S. The kirkendall effect for engineering oxygen vacancy of hollow Co_3O_4 nanoparticles toward high-performance portable zinc-air batteries. *Angew. Chem., Int. Ed.* **2019**, *58*, 13840−13844.
(46) Wang, Q.; Shang, L.; Shi, R.; Zhang, X.; Waterhouse, G. I. N.; Wu, L.-Z.; Tung, C.-H.; Zhang, T. 3D carbon nanoframe scaffold-immobilized Ni_3FeN nanoparticle electrocatalysts for rechargeable zinc-air batteries' cathodes. *Nano Energy* **2017**, *40*, 382−389.
(47) Park, J.; Risch, M.; Nam, G.; Park, M.; Shin, T. J.; Park, S.; Kim, M. G.; Shao-Horn, Y.; Cho, J. Single crystalline pyrochlore nanoparticles with metallic conduction as efficient bi-functional oxygen electrocatalysts for Zn-air batteries. *Energy Environ. Sci.* **2017**, *10*, 129−136.
(48) Luo, M.; Zhao, Z.; Zhang, Y.; Sun, Y.; Xing, Y.; Lv, F.; Yang, Y.; Zhang, X.; Hwang, S.; Qin, Y.; Ma, J.-Y.; Lin, F.; Su, D.; Lu, G.; Guo, S. PdMo bimetallene for oxygen reduction catalysis. *Nature* **2019**, *574*, 81−85.
(49) Huang, W.; Li, J.; Liao, X.; Lu, R.; Ling, C.; Liu, X.; Meng, J.; Qu, L.; Lin, M.; Hong, X.; Zhou, X.; Liu, S.; Zhao, Y.; Zhou, L.; Mai, L. Ligand modulation of active sites to promote electrocatalytic oxygen evolution. *Adv. Mater.* **2022**, *34*, 2200270.
(50) Zhang, Z.; Feng, C.; Li, X.; Liu, C.; Wang, D.; Si, R.; Yang, J.; Zhou, S.; Zeng, J. In-situ generated high-valent iron single-atom catalyst for efficient oxygen evolution. *Nano Lett.* **2021**, *21*, 4795−4801.
(51) Fan, K.; Chen, H.; Ji, Y.; Huang, H.; Claesson, P. M.; Daniel, Q.; Philippe, B.; Rensmo, H.; Li, F.; Luo, Y.; Sun, L. Nickel-vanadium monolayer double hydroxide for efficient electrochemical water oxidation. *Nat. Commun.* **2016**, *7*, 11981.
(52) Gao, M.; Sheng, W.; Zhuang, Z.; Fang, Q.; Gu, S.; Jiang, J.; Yan, Y. Efficient water oxidation using nanostructured α-nickel-hydroxide as an electrocatalyst. *J. Am. Chem. Soc.* **2014**, *136*, 7077−7084.
(53) Bai, L.; Hsu, C.-S.; Alexander, D. T. L.; Chen, H. M.; Hu, X. Double-atom catalysts as a molecular platform for heterogeneous oxygen evolution electrocatalysis. *Nat. Energy* **2021**, *6*, 1054−1066.
(54) Man, I. C.; Su, H.-Y.; Calle-Vallejo, F.; Hansen, H. A.; Martínez, J. I.; Inoglu, N. G.; Kitchin, J.; Jaramillo, T. F.; Nørskov, J. K.; Rossmeisl, J. Universality in Oxygen Evolution Electrocatalysis on Oxide Surfaces. *ChemCatChem* **2011**, *3*, 1159−1165.
(55) Dronskowski, R.; Bloechl, P. E. Crystal orbital Hamilton populations (COHP): energy-resolved visualization of chemical bonding in solids based on density-functional calculations. *J. Phys. Chem.* **1993**, *97*, 8617−8624.

https://doi.org/10.1021/jacs.2c12933
J. Am. Chem. Soc. 2023, 145, 3647−3655